applied optics

Optimal wavelength selection strategy in temporal phase unwrapping with projection distance minimization

Hui Li,[1,2,3] Yan Hu,[1,2,3] Tianyang Tao,[1,2,3] Shijie Feng,[1,2,3] Minliang Zhang,[1,2,3] Yuzheng Zhang,[1,2,4] and Chao Zuo[1,2,3,*]

[1]School of Electronic and Optical Engineering, Nanjing University of Science and Technology, No. 200 Xiaolingwei Street, Nanjing, Jiangsu Province 210094, China
[2]Jiangsu Key Laboratory of Spectral Imaging & Intelligent Sense, Nanjing, Jiangsu Province 210094, China
[3]Smart Computational Imaging Laboratory (SCILab), Nanjing University of Science and Technology, Nanjing, Jiangsu Province 210094, China
[4]Ministerial Key Laboratory of JGMT, Nanjing University of Science and Technology, Nanjing, Jiangsu Province 210094, China
*Corresponding author: surpasszuo@163.com

Received 7 November 2017; accepted 16 February 2018; posted 22 February 2018 (Doc. ID 297746); published 22 March 2018

Micro Fourier transform profilometry (μFTP) is a recently developed computational framework for high-speed dynamic 3D shape measurement of transient scenes based on fringe projection. It has been demonstrated that by using high-frame-rate fringe projection hardware, μFTP can achieve accurate, denser, unambiguous, and motion-artifact-free 3D reconstruction at a speed up to 10,000 Hz. μFTP utilizes a temporal phase unwrapping algorithm, so-called projection distance minimization (PDM), in which multiple wavelengths are used to solve the phase ambiguity optimally in the maximum-likelihood sense. However, it has been found that the choice of the wavelengths is essential to the unambiguous measurement range as well as the unwrapping reliability in the presence of noise. In this work, the relations between the wavelength combination and the noise resistance ability of PDM are analyzed and investigated in detail by analytical, emulational, and experimental means. This leads to a qualitative conclusion that the noise resistance ability of PDM is fundamentally determined by the value of each item in wavelength ratio: a smaller value of each item in wavelength ratio means better noise resistance ability in phase unwrapping. Our result provides a guideline for optimal wavelengths selection in order to improve the noise resistance ability of a practical fringe projection system. Simulations and experiments based on a microscopic fringe projection system are demonstrated to validate the correctness of our conclusion.

OCIS codes: (120.5050) Phase measurement; (120.0120) Instrumentation, measurement, and metrology; (150.6910) Three-dimensional sensing; (330.1400) Vision - binocular and stereopsis.

https://doi.org/10.1364/AO.57.002352

1. INTRODUCTION

Fringe projection profilometry (FPP) is widely employed in the fields of industrial inspection, quality control, machine vision, entertainment, and biomedicine due to its non-contact nature and full-field performance in 3D shape measurement [1,2]. With the rapid development of the digital light processing (DLP) technology, the measurement scenes of FPP not only contain the static objects, but also extend to the motion or deformation of dynamic objects. In FPP, phase-shifting profilometry (PSP) [3–6] and Fourier transform profilometry (FTP) [7–10] are the two mainstream techniques.

PSP has the advantages of high accuracy, robustness, and flexibilities when coping with complex scenes that contain sharp edges or varying surface properties. Theoretically, the minimum number of projection patterns for getting the wrapped phase in PSP is three. In order to eliminate the ambiguity of wrapped phase, a reliable phase unwrapping procedure should be applied to obtaining the continuous phase map [11–13]. Spatial phase unwrapping algorithms [14–16] use spatial phase constraint to unwrap the phase, but the ambiguity of phase cannot be eliminated correctly when there are multiple isolated objects or abrupt surface changes in the measurement scenes. Temporal phase unwrapping algorithms [17–20] can solve this problem, but additional patterns are required to get the extra phase information for phase unwrapping. Obviously, for dynamic 3D measurement, additional projected patterns will increase more potential motion artifacts. To decrease the influence caused by the object motion, researchers have

proposed many methods. *Zuo et al.* [21] and *Liu et al.* [22] decreased the pattern number to five by utilizing the average light of the three fringe patterns and the dual-frequency pattern scheme, respectively. *Zuo et al.* [23] also presented a "2 + 2" phase shifting method in which four patterns are needed. To further reduce the sensitivity to dynamic scenes, adding speckle in the fringe pattern [24] and exploiting geometry constraint in a multi-camera system [25] are two methods which can calculate the absolute phase of a complex surface using just three fringe patterns. Another commonly used approach of FPP is FTP [26], by which only one fringe pattern is sufficient to retrieve the phase. However, when the measured scene contains sharp edges, discontinuities, or large surface reflectivity variations, the spectrum overlapping problem will preclude high-accuracy phase reconstruction. Modified FTP, which uses another π-shift fringe pattern [27], has been proposed to address this problem. But the phase information is encoded in two sinusoidal fringes with π-shift FTP, thus the sensitivity to object motion is increased. Although these above methods can reduce the pattern number, the maximum frame rate of current dynamic FPP 3D imaging has far been limited to a speed less than 1000 Hz. Recently, *Zuo et al.* [28] have proposed micro Fourier transform profilometry (μFTP), in which two pattern projections are needed to recover an accurate, unambiguous, and dense 3D point cloud. Furthermore, the phase information is encoded within only one single high-frequency fringe image, making the motion artifacts minimized. By using high-frame-rate hardware, this technique realizes capture of 3D shape of non-repetitive, time evolving events at up to 10,000 fps.

In μFTP, n ($n \geq 2$) high-frequency sinusoidal fringe patterns with slightly different wavelengths (fringe pitches) are projected to the measurement scene. Between every two sinusoidal fringe patterns, a "white" pattern with all micro mirror in the DMD at the "on" state is inserted in the pattern sequence. n wrapped phase maps can be recovered based on the background-normalized Fourier transform profilometry (BNFTP). Then temporal phase unwrapping with projection distance minimization (PDM) is applied to eliminate the ambiguity of the wrapped phase by exploiting the information of the neighboring wrapped phase maps with different frequency. This technique is validated as the optimal multi-frequency temporal phase unwrapping method. However, we find that the wavelength combination influences the noise resistance ability of phase unwrapping greatly in PDM; even if each wavelength only changes one or two pixels, the noise resistance ability will be quite different. This phenomenon makes it very prudent to design the wavelength combination in μFTP for improving the noise resistance ability of the practical fringe projection system.

In this work, we analyze the relations between the wavelength combination and the noise resistance ability in PDM. This problem is transformed into a geometric distance comparison problem for intuitive observation and analysis. The minimum distance between the points which represent the different fringe orders can reflect the noise resistance ability of the different wavelength combination. Finally, we obtain a qualitative conclusion: the noise resistance ability of the wavelength combination is determined by the value of each item in wavelength ratio: a smaller value of each item in wavelength ratio means better noise resistance ability in PDM. This conclusion provides an optimal wavelength selection strategy for PDM. Both simulations and experiments based on a microscopic fringe projection system are carried out. The results prove the correctness of our conclusion.

2. PRINCIPLE

A. Micro Fourier Transform Profilometry

μFTP projects n ($n \geq 2$) high-frequency sinusoidal fringe patterns with slightly different wavelengths (fringe pitches) $\{\lambda_1, \lambda_2, \cdots \lambda_n\}$ to the measured scenes. Between every two sinusoidal fringe patterns, a "white" pattern with all mirror in the DMD at the "on" state is inserted in the pattern sequence. Thus, there are $2n$ patterns in total that need to be projected. For μFTP, the fringe wavelength combination $\{\lambda_1, \lambda_2, \cdots \lambda_n\}$ must meet the following two conditions: (1) λ_i should be sufficiently small (frequency is enough high) as required for successful phase retrieval in convention FTP; (2) the least common multiple (LCM) of the fringe wavelength combination should be greater than the total pixel number in the axis along which the sinusoidal intensity value varies. So that the phase ambiguities can be theoretically excluded. The captured images are processed sequentially, with $2n$-frame sliding windows moving across all the images. Considering $2n$-frame within a window centered on the current frame at given time point (t_0), we have n sinusoid images $\{I_1, I_2, \cdots, I_n\}$ and corresponding n white images $\{I_1^b, I_2^b, \cdots, I_n^b\}$. From these image pairs, n wrapped phase maps $\{\phi_1, \phi_2, \cdots, \phi_n\}$ can be recovered based on the BNFTP.

In BNFTP, the zero frequency term as well as the effect of surface reflectivity variations can be effectively removed:

$$I_d(x^c, y^c) = \frac{2I_1 - I_1^b}{I_1^b + \gamma} = \cos[2\pi f_0 x^c + \phi(x^c, y^c)], \quad (1)$$

where (x^c, y^c) is the pixel coordinate in the camera space, γ is a small constant to prevent divide-by-zero error, I_1 is the intensity of the captured sinusoidal fringe image, I_1^b is the captured white image, f_0 is the carrier frequency of the captured fringe image, and ϕ is the phase containing the depth information of the measured object. Then the Fourier transform is applied on the background normalized image I_d to extract the phase information. With the subtraction and normalization of the white image, the effect of zero-order as well as surface reflectivity variations is removed before the Fourier transform, so that the spectrum overlapping in the frequency domain can be prevented or at least significantly alleviated.

For μFTP, the phase of the current time point (t_0) is unwrapped temporally by exploiting information from neighboring frames based on an algorithm so-called PDM. The basic idea of PDM is to determine the optimum fringe order combination $\{k_1, k_2, \cdots, k_n\}$ (for each wrapped phase map $\{\phi_1, \phi_2, \cdots, \phi_n\}$) which the corresponding unwrapped phase value combination $(\Phi_1, \Phi_2, \cdots, \Phi_n)$ is "closest" (in the Euclidean sense) to the following straight line in dimension n:

$$\Phi_1\lambda_1 = \Phi_2\lambda_2 = \ldots = \Phi_n\lambda_n. \quad (2)$$

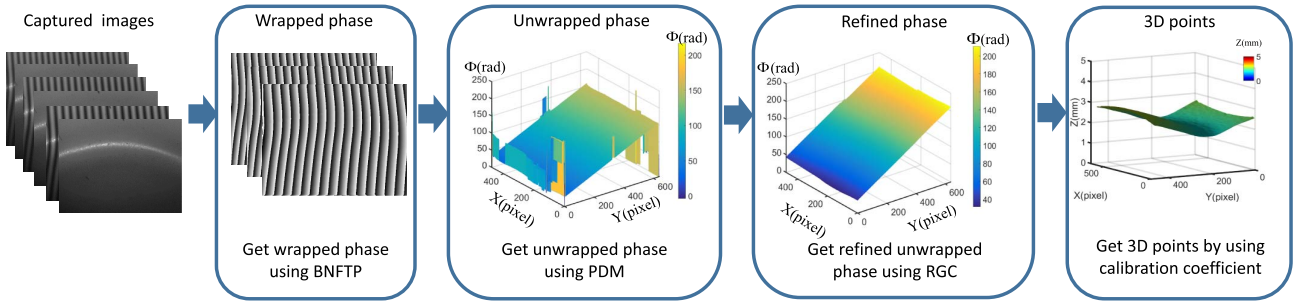

Fig. 1. Flowchart of μFTP.

Then the initial unwrapped phase map corresponding to t_0 is further refined in the spatial domain with a reliability-guided compensation algorithm to correct the fringe order errors induced by low fringe quality and no negligible frame-by-frame object motion. Finally, the refined unwrapped phase is used to establish the projector-camera pixel correspondence, and the 3D coordinates of the object surface at time t_0 can be reconstructed based on the relationship derived from the parameters for the triangulation configuration of the projector and the camera. The flowchart of μFTP is shown in Fig. 1.

B. Temporal Phase Unwrapping with Projection Distance Minimization

PDM is proposed to address the multi-frequency temporal phase unwrapping in an optimum way. Suppose we have n relative phase maps arranged in a vector $\boldsymbol{\phi} = [\phi_1, \phi_2, \cdots, \phi_n]^T$, characterized by the fringe wavelengths (fringe pitches) $\boldsymbol{\lambda} = [\lambda_1, \lambda_2, \cdots, \lambda_n]^T$, the corresponding unwrapped phase maps $\boldsymbol{\Phi} = [\Phi_1, \Phi_2, \cdots, \Phi_n]^T$ can be represented as

$$\boldsymbol{\Phi} = \boldsymbol{\phi} + 2\pi\mathbf{k}, \tag{3}$$

where $\mathbf{k} = [k_1, k_2, \cdots, k_n]^T$ is the integer fringe order vector. The task of phase unwrapping is to determine the fringe orders k from the knowledge of wrapped phase vector $\boldsymbol{\phi}$ only, and the continuous phase maps $\boldsymbol{\Phi}$ can be recovered by Eq. (3). To achieve this, the fringe wavelength combination $\boldsymbol{\lambda}$ should be properly chosen so that the phase $\boldsymbol{\phi}$ can be successfully unwrapped without ambiguities within the desired measurement range. This relies on the fact that for fringe wavelengths $\boldsymbol{\lambda} = [\lambda_1, \lambda_2, \cdots, \lambda_n]^T$, their least common multiple $\mathrm{LCM}(\lambda_1, \lambda_2, \cdots, \lambda_n)$ determines the maximum range on the absolute phase axis within which each fringe order combination for wrapped phase values is unique. Considering the projection pattern has W pixels in the horizontal axis along which the sinusoidal intensity value varies (the pixels in the same column all have equal intensity), the condition should be satisfied to exclude ambiguity:

$$\mathrm{LCM}(\lambda_1, \lambda_2, \cdots, \lambda_n) \geq W. \tag{4}$$

All unwrapped phase values can be connected with the corresponding projector coordinate x_p through the following relation:

$$\boldsymbol{\Phi} \circ \boldsymbol{\lambda} = 2\pi x_p \equiv t, \tag{5}$$

where $\circ$ is the Hadamard product (entrywise product). Equation (5) suggests that the trajectory of continuous phase values $(\Phi_1, \Phi_2, \cdots, \Phi_n)$ forms a straight line passing through the origin in dimension n. The direction vector of the line is $\boldsymbol{\lambda}^{-1} = \left[\frac{1}{\lambda_1}, \frac{1}{\lambda_2}, \cdots, \frac{1}{\lambda_n}\right]^T$ and the line can be parameterized by parameter t. For a given set of wrapped phase values $\boldsymbol{\phi} = [\phi_1, \phi_2, \cdots, \phi_n]^T$, the problem of temporal phase unwrapping is recast as finding the integer fringe order vector $\mathbf{k} = [k_1, k_2, \cdots, k_n]^T$ so that the final unwrapped phase values $\boldsymbol{\Phi} = [\Phi_1, \Phi_2, \cdots, \Phi_n]^T$ calculated from Eq. (3) can precisely fall on the straight line described by Eq. (5). Since the ambiguity in the projector space is ruled out by condition Eq. (4), there should be only one qualified fringe order vector k within the range $0 \leq x_p < W$ [28].

However, in practice, there are many factors, such as non-sinusoidality of the pattern intensity, random noise of the projector and the camera, and object motion in the measurement process, that may induce errors in obtained wrapped phase maps. In such cases, the unwrapped phase values $\boldsymbol{\Phi} = [\Phi_1, \Phi_2, \cdots, \Phi_n]^T$ calculated from Eq. (3) may never precisely fall on the straight line described by Eq. (5) for all possible fringe order vectors. To solve the phase unwrapping problem optimally in the presence of noise, the fringe orders that make the unwrapped phase values $\boldsymbol{\Phi} = [\Phi_1, \Phi_2, \cdots, \Phi_n]^T$ closest to the straight line should be chosen. Thus, the distance from the point $(\Phi_1, \Phi_2, \cdots, \Phi_n)$ to the line in Euclidean geometry should be calculated to quantify how close they are. The distance d from the point to the line can be calculated by Eq. (6):

$$\begin{aligned} d^2 &= \boldsymbol{t}^T\boldsymbol{t}, \\ \boldsymbol{t} &= \left(\sum_{i=1}^{n}(1\lambda_i^2)\right)^{-1}\sum_{i=1}^{n}\Phi_i\lambda_i\boldsymbol{\lambda}^{-1} - \boldsymbol{\Phi}. \end{aligned} \tag{6}$$

Select the fringe order vector that produces the minimum d_i^2 (denoted as $d_{\min}^2$) as the optimum solution k_{opt}. Meanwhile, the corresponding unwrapped phase values $\boldsymbol{\Phi}_{\mathrm{opt}}$ can be obtained by Eq. (3).

C. Optimum Choice of Wavelength Combination

As mentioned in Sections 2.A and 2.B, two prerequisites must be satisfied when choosing the fringe wavelengths for μFTP: (1) λ_i should be sufficiently small, and (2) $\mathrm{LCM}(\lambda_1, \lambda_2, \cdots \lambda_n) \geq W$. Therefore, the phase ambiguities can be theoretically excluded. Obviously, the wavelength combination that satisfies both of the prerequisites is not unique. We find that the choice of wavelength combination makes great influence on the noise resistance ability in PDM.

To analyze this problem intuitionally, we rewrite Eqs. (3) and (5) as follows:

$$\begin{cases} \phi_1 = \frac{2\pi}{\lambda_1}x - 2\pi k_{1,i}, \\ \phi_2 = \frac{2\pi}{\lambda_2}x - 2\pi k_{2,i}, \\ \quad \cdots, \\ \phi_n = \frac{2\pi}{\lambda_n}x - 2\pi k_{n,i}, \end{cases} \tag{7}$$

where $1 \le i \le N$, N is the total number of all the possible fringe orders, which is finite. The system of equations in Eq. (7) describes some parameterized straight lines in dimension n where x is the line parameter. It may be interpreted as follows: due to the shared common independent variable x, all observable values of wrapped phase are limited to the intersection of a set of lines in dimension n [29]. The number of the straight lines is N. The direction vector of these lines is $[\frac{2\pi}{\lambda_1}, \frac{2\pi}{\lambda_2}, \cdots, \frac{2\pi}{\lambda_n}]^T$.

However, in practical measurements, the wrapped phase point influenced by the noise will deviate from the line corresponding to the correct fringe orders. In this case, the fringe orders corresponding to the closest line with the wrapped phase point should be chosen to unwrap the phase. Nevertheless, once the noise makes the wrapped phase point deviate from the line corresponding to the correct fringe orders so far that the wrapped phase point is closer to the line corresponding to another fringe order, the wrong unwrapped phases will be obtained. Obviously, the minimum distance between the lines is the parameter to judge the noise resistance ability of the wavelength combination. Larger distance between the lines makes better noise resistance ability of the wavelength combination. Therefore, the problem of the relations between the wavelength combination and the noise resistance ability becomes a geometric distance comparison problem.

Here, we take the wavelength combination {4, 6, 10} as an example. The LCM of the wavelength combination is 60 and the number of all the possible fringe orders is 22. Figure 2(a) is the distribution of all the wrapped phase points in the wrapped phase space without noise and these points form the straight lines. The lines are parallel to each other, which verifies Eq. (7). For a more intuitive observation, we project these lines onto the plane perpendicular to them, as shown in Fig. 2(b). From this perspective, these lines become points because they have the same direction vectors, and the distances between the points on this projection plane are as same as the distances between the lines. To analyze the relations between the distance of the points and the wavelength combination, we project the lines onto the $\phi_1\phi_2$, $\phi_1\phi_3$, and $\phi_2\phi_3$ planes, respectively, which are shown in Figs. 2(c)–2(e). It can be seen that the projections of these lines on the projection planes are still parallel to each other. It is worth noting that the intersections of the lines on the projection plane and the coordinate axes ϕ_1, ϕ_2, ϕ_3 divide the coordinate axes into 2, 3, and 5 parts on average, respectively. It is the same as the value of each item in wavelength ratio 2:3:5. Therefore, the value of each item in wavelengths ratio determines how many parts of the coordinate axes on each projection plane will be divided on average. The more parts of the coordinate axes being divided, the shorter distance between the lines on the projection plane, which indicates that the distance between the lines in the 3D space will also be shorter and the noise resistance ability of the wavelength combination will be worse. Based on the above analysis, we can obtain a qualitative conclusion that the noise resistance ability of the wavelength combination is determined by the value of each item in wavelength ratio: a smaller value of each item in wavelength ratio means better noise resistance ability in phase unwrapping.

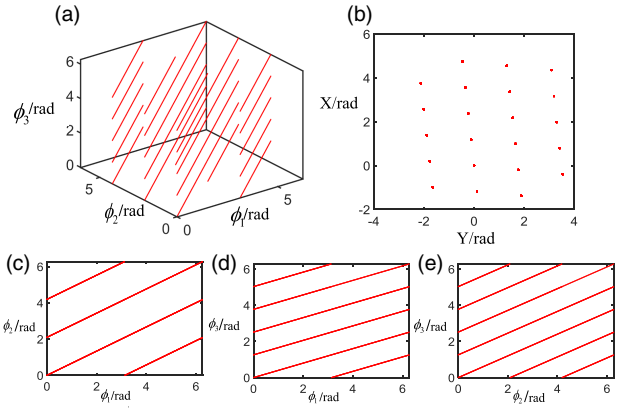

Fig. 2. Example of the wrapped phases distribution in the wrapped phases space (the pixel of each wavelength is {4, 6, 10}). (a) The wrapped phases distribution in the 3D space. (b) The projection of the wrapped phases on the plane perpendicular to direction vectors of the straight lines. (c)–(e) The projection of the wrapped phases on the $\phi_1\phi_2$ plane, $\phi_1\phi_3$ plane, and $\phi_2\phi_3$ plane, respectively.

We illustrate this conclusion by designing the optimal wavelength combination for a microscopic fringe projection system. The pixel number of the projector in the axis along which the sinusoidal intensity value varies is 608. For the balance of the robustness of phase unwrapping and the influence of the object motion, using three wavelengths is a good choice. First, in order to guarantee the measurement accuracy of conventional FTP, the fringe number is at least 30. In addition, the fringes cannot be too dense for keeping the fringe contrast, thus the fringe number is limited to 50. Therefore, the wavelength range is between 13 and 21 pixels. Second, the LCM of three wavelengths must be larger than or equaled to 608. We can list the following representative wavelength combinations, which are shown in Table 1. The four wavelength combinations all satisfy the prerequisites. We also list their wavelength ratio and the LCM of the wavelengths in Table 1. According to the conclusion that smaller value of each item in wavelength ratio means better noise resistance ability, the order of the noise resistance ability of the four wavelength combinations from

Table 1. Four Wavelength Combinations that Meet the Prerequisites

Index	Wavelength Combination	Wavelength Ratio	LCM of the Wavelength
①	{13 15 17}	13:15:17	3315
②	{14 16 18}	7:8:9	1008
③	{15 18 21}	5:6:7	630
④	{16 17 18}	16:17:18	2448

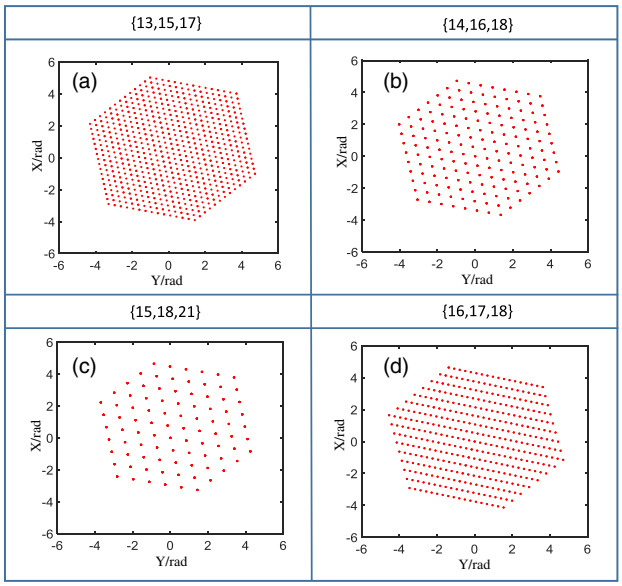

Fig. 3. Distributions of the points on the plane perpendicular to the direction vectors with different wavelength combinations. (a)–(d) The distances between the neighboring points of wavelength combination {13, 15, 17}, {14, 16, 18}, {15, 18, 21}, and {16, 17, 18}, respectively.

strong to weak should be ③②①④. Moreover, the noise resistance ability of combination ③ and ② should be much stronger than combination ① and ④, because their values of each item in wavelength ratio are much smaller than those of two combinations. This order of the noise resistance ability is based on our proposed conclusion. We can verify the correctness of this order by observing the points distribution on the plane perpendicular to the straight lines of the four wavelength combinations, as shown in Fig. 3.

Figures 3(a)–3(d) correspond to the wavelength combination of ①–④, respectively. It can be seen from Fig. 3 that the points of combination ② and ③ are obviously sparser than those of ① and ④, and the points of ③ are sparsest. In addition, the distribution of the points is regular hexagon, thus the distances between the two neighboring points only exist three possibilities and the smallest distance is the parameter to evaluate the noise resistance ability of the corresponding wavelength combination. We calculate out these distances, which are shown in Table 2 and Fig. 4. Figures 4(a)–4(d) correspond to the distance of the neighboring points with wavelength combination of ①–④.

From Table 2 and Fig. 4, we can obtain that the order of the minimum distance between the neighboring points from large

Table 2. Distances between the Neighboring Points with Different Wavelength Combinations

Index	Wavelength Combination		Distance		Shortest Distance
①	{13 15 17}	0.3462	0.3194	0.3650	0.3194
②	{14 16 18}	0.6457	0.6023	0.6830	0.6023
③	{15 18 21}	0.8671	0.7869	0.9289	0.7869
④	{16 17 18}	0.3024	0.5859	0.5235	0.3024

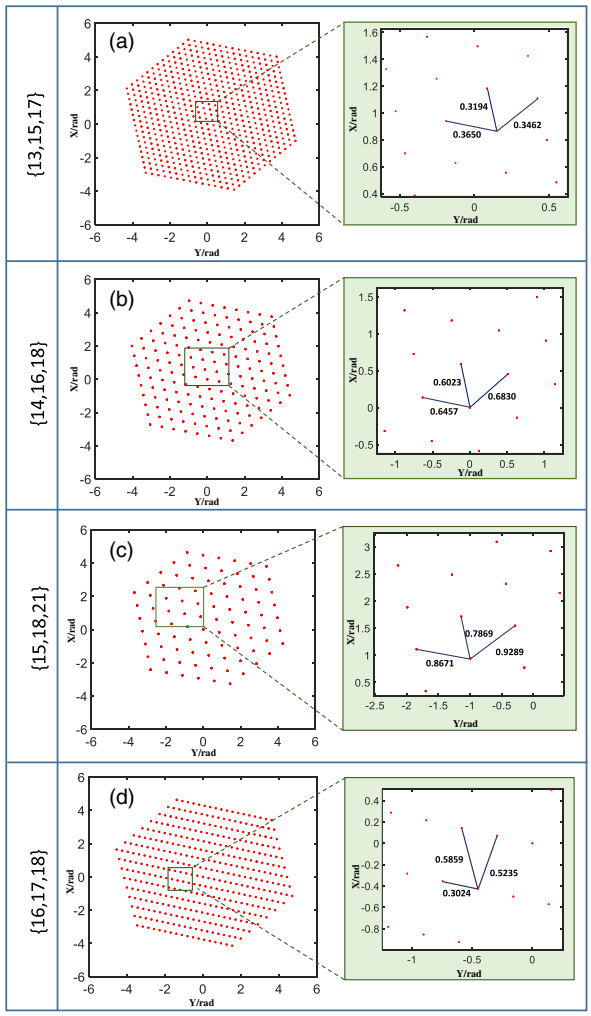

Fig. 4. Distances between the neighboring points on the plane perpendicular to the direction vectors with different wavelength combinations. (a)–(d) The distances between the neighboring points of wavelength combination {13, 15, 17}, {14, 16, 18}, {15, 18, 21}, and {16, 17, 18}, respectively.

to small is ③②①④, which is consistent with the order we inferred according to the proposed conclusion. This proves the correctness of our conclusion.

3. SIMULATIONS

We performed the simulations to compare the performance of the four wavelength combinations when Gaussian noise presents. In simulations, we use PDM to unwrap the wrapped phase maps. The Gaussian noise is used to emulate the camera noise effect in real experiments. We compare the four wavelength combinations under the situation of zero-mean Gaussian noise with variance of 0.0005, 0.005, and 0.01, respectively. The results are shown in Fig. 5. When the noise variance is 0.0005, the phase unwrapping success rate of four wavelength combinations are all 100%. When the noise variance is increased to 0.005, combinations ① and ④ are unable to unwrap all the phases correctly while combinations ② and ③

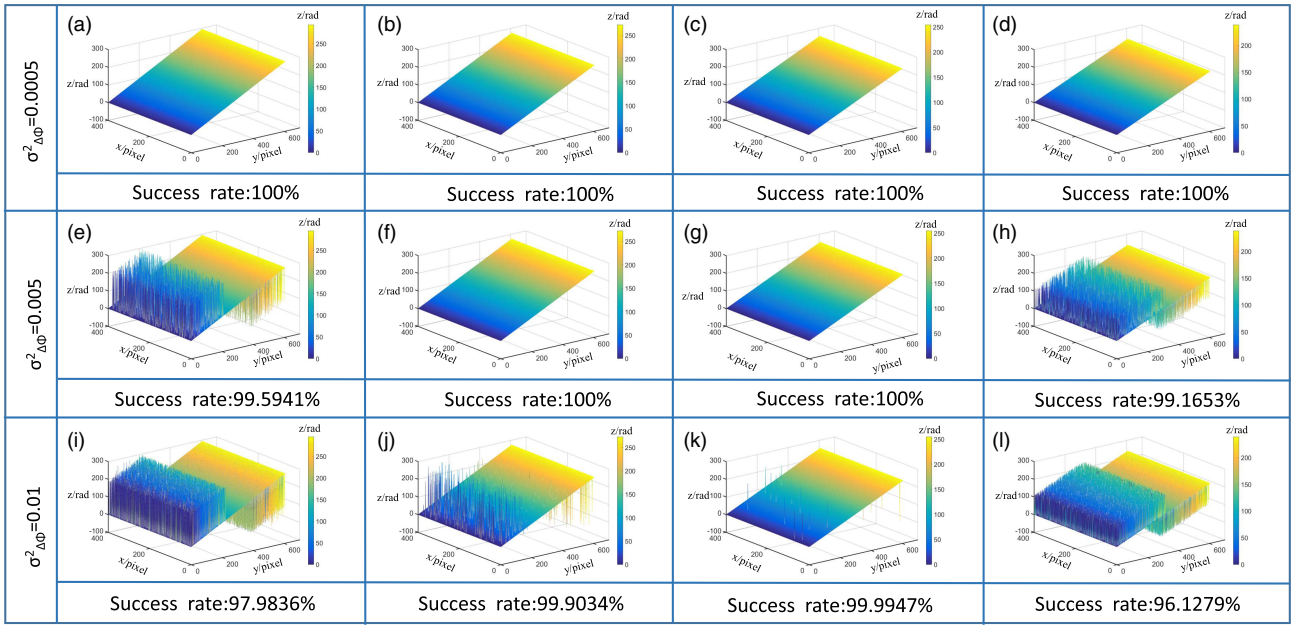

Fig. 5. Comparison of the phase unwrapping success rate between the four wavelength combinations under zero-mean Gaussian noise with $\sigma^2_{\Delta\phi} = 0.0005, 0.005, 0.01$. (a)–(d) The unwrapped phases and success rate of the wavelength combination ①–④ under $\sigma^2_{\Delta\phi} = 0.0005$. (e)–(h) The unwrapped phases and success rate of the wavelength combination ①–④ under $\sigma^2_{\Delta\phi} = 0.005$. (i)–(l) The unwrapped phases and success rate of the wavelength combination ①–④ under $\sigma^2_{\Delta\phi} = 0.01$.

remain 100% success rate. When the noise variance is increased to 0.01, the four wavelength combinations all have phase unwrapping error. But obviously, the success rate of combination ③ is the highest, and the success rate order from high to low is ③②①④. The simulation results further demonstrate the correctness of our proposed conclusion. The wrapped phase distributions of the projection on the plane perpendicular to the direction vectors of the four wavelength combinations under the zero-mean Gaussian noise with variance of 0.005 are shown in Fig. 6. Figures 6(a)–6(d) correspond to the wavelength combination of ①–④, respectively. It can be seen that the wrapped phase point deviates from the former places shown in Fig. 3 because of the noise influence. The advantage of far distance between the points in the presence of noise is obvious. Combination ③ corresponding to Fig. 6(c) has the minimal possibility of phase unwrapping error compared with the other three wavelength combinations.

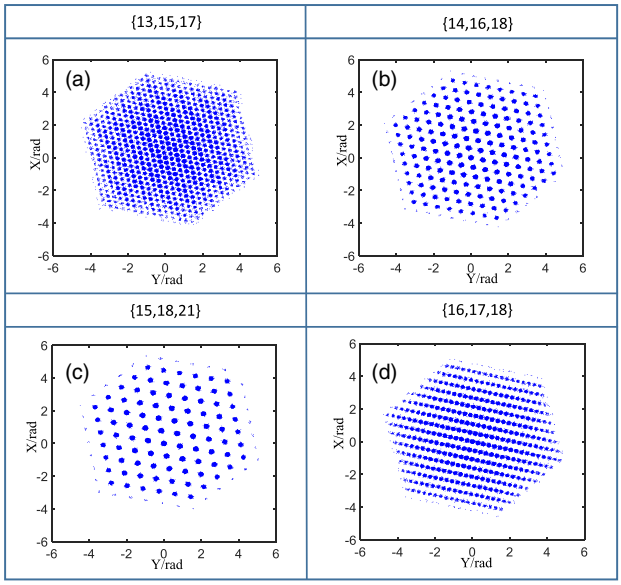

Fig. 6. Distributions of the wrapped phases points on the plane perpendicular to the direction vectors with different wavelength combinations under Gaussian noise with $\sigma^2_{\Delta\phi} = 0.0005$. (a),(b) The distribution of the wrapped phases of wavelength combination {13, 15, 17}, {14, 16, 18}, {15, 18, 21}, and {16, 17, 18}, respectively.

4. EXPERIMENTS

To validate the conclusions we obtained, experiments were conducted with the microscopic fringe projection system composed of a Greenough-type stereo microscope, a digital projector (LightCrafter based on a DLP3000 DMD chip) with resolution of 608 × 684, and a high-speed CMOS camera (Basler acA640-750 μm) with resolution of 640 × 480 [30]. The profile of the system is shown in Fig. 7.

A. Measurements with Different Wavelength Combinations

To compare the performance of the four wavelength combinations, we first measured a ceramic plate by μFTP. This ceramic plate has the precision of 1 μm, thus it is qualified to serve as a standard planar surface. In order to highlight the comparative effect, we artificially increased the intensity noise by reducing the camera exposure. The unwrapped phase maps of the ceramic plate corresponding to the four different wavelength

Fig. 7. Microscopic fringe projection system.

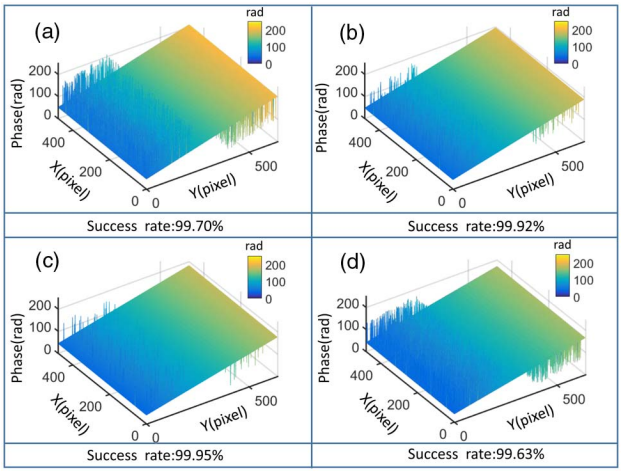

Fig. 8. Unwrapped phase maps of the ceramic plate. (a)–(d) Unwrapped phase maps of the ceramic plate of wavelength combination ①–④, respectively.

combinations and their success rates are shown in Fig. 8. Figures 8(a)–8(d) correspond to the wavelength combinations of ①–④. Obviously, the success rate of combination ③ is the highest, and the success rate order from high to low is ③②①④. This result is consistent with the simulation. So that we can get the conclusion that for this experimental system, the wavelength combination ③ can provide the best ability of noise resistance.

We also measured an earphone diaphragm to further prove the conclusion. The 3D reconstruction results corresponding to the four wavelength combinations of the earphone diaphragm are shown in Fig. 9. The performance of the four wavelength combinations is the same as the ceramic plate. Obviously,

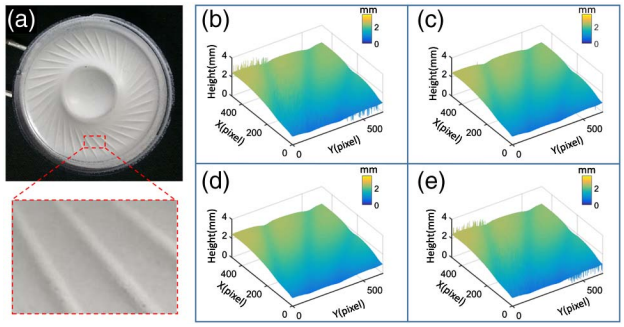

Fig. 9. 3D reconstruction results of the earphone diaphragm. (a) The measured part of the earphone diaphragm. (b)–(e) The 3D reconstruction results of the earphone diaphragm of wavelength combination ①–④, respectively.

wavelength combination ③ performs best, which is consistent with our conclusions.

B. Static Measurement with the Optimal Wavelength Combination

Next we tested a BGA chip to show the performance of the optimal wavelength combination {15, 18, 21} for the measurement object with complex surface. Figure 10(a) is the measured BGA chip. The area in the yellow dotted line is the measurement part. The reconstruction result is shown in Fig. 10(b). We could clearly recognize the spherical structures representing the balls which are very smooth and well reconstructed. Figure 10(c) is the cross section corresponding to the red dashed line in Fig. 10(b). The obtained 3D data may provide sufficient information to analyze the features and to detect the defect on the balls.

C. Dynamic Measurement with the Optimal Wavelength Combination

Finally, we tested an earphone diaphragm vibrated with different frequencies to illustrate the performance of optimal wavelength combination for measuring dynamic scenes. The vibration frequency of the earphone diaphragm was set as 1 Hz, 5 Hz, and 10 Hz, respectively. The measurement results are shown in Fig. 11. Figure 11(a) is the picture of the earphone

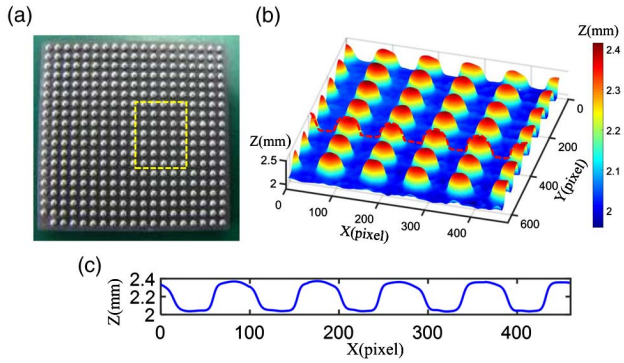

Fig. 10. 3D reconstruction results of the BGA chips. (a) The measured BGA chips. (b) Reconstructed 3D data corresponding to the area in the yellow dotted line of (a). (c) A cross section corresponding to the red dotted line in (b).

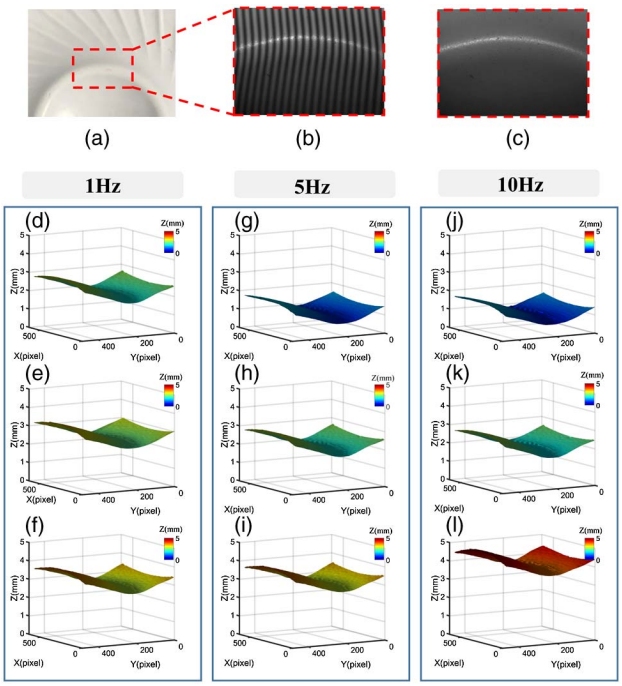

Fig. 11. 3D reconstruction results of the vibrating earphone diaphragm. (a) The measurement part of the earphone diaphragm, which is the area in the red dashed box. (b) The image captured by the camera when the projector projects high-frequency sinusoidal fringe pattern. (c) The image captured by the camera when the projector projects the white pattern. (d)–(f) The 3D reconstruction of the earphone at different heights with the vibration frequency of 1 Hz (see Visualization 1). (g)–(i) The 3D reconstruction of the earphone at different heights with the vibration frequency of 5 Hz (see Visualization 2). (j)–(l) The 3D reconstruction of the earphone at different heights with the vibration frequency of 10 Hz (see Visualization 3).

diaphragm and the area in the red dashed box is the measured part. Figures 11(b) and 11(c) are the images captured by the camera when the projector projected a white image and high-frequency sinusoidal fringe pattern, respectively. Figures 11(d)–11(f), 11(g)–11(i), and 11(j)–11(l) are the reconstruction results of the earphone diaphragm at different heights with 1 Hz, 5 Hz, and 10 Hz vibration frequencies, respectively. The corresponding videos are presented in Visualization 1, Visualization 2, and Visualization 3, respectively. The measurement results of the vibrating earphone diaphragm demonstrate the robustness of the optimal wavelength combination strategy for measuring dynamic scenes.

5. CONCLUSION

This paper analyzes the relations between the wavelength combination and the noise resistance ability in PDM. By analytical, emulational, and experimental means, we obtain a qualitative conclusion: the noise resistance ability of the wavelength combination is determined by the value of each item in wavelength ratio and a smaller value of each item in wavelength ratio means better noise resistance ability in phase unwrapping. This conclusion provides the optimal strategy for wavelength combination selection in PDM in order to improve the noise resistance ability of the fringe projection system. However, this work only stayed in qualitative analysis. Further research about this problem with quantitative calculation will also be carried out in the future work.

Funding. National Key R&D Program of China (2017YFF0106403); National Natural Science Foundation of China (NSFC) (111574152, 61705105, 61722506); Final Assembly "13th Five-Year Plan" Advanced Research Project of China (30102070102); Outstanding Youth Foundation of Jiangsu Province of China (BK20170034); National Defense Science and Technology Foundation of China (0106173); "Six Talent Peaks" Project of Jiangsu Province, China (2015-DZXX-009); "333 Engineering" Research Project of Jiangsu Province, China (BRA2016407); Fundamental Research Funds for the Central Universities (30916011322, 30917011204); Open Research Fund of Jiangsu Key Laboratory of Spectral Imaging & Intelligent Sense (3091601410414); China Postdoctoral Science Foundation (2017M621747); Jiangsu Planned Projects for Postdoctoral Research Funds (1701038A).

REFERENCES

1. S. S. Gorthi and P. Rastogi, "Fringe projection techniques: whither we are?" Opt. Lasers Eng. **48**, 133–140 (2010).
2. Z. Zhang, "Review of single-shot 3D shape measurement by phase calculation-based fringe projection techniques," Opt. Lasers Eng. **50**, 1097–1106 (2012).
3. V. Srinivasan, H.-C. Liu, and M. Halioua, "Automated phase-measuring profilometry of 3-D diffuse objects," Appl. Opt. **23**, 3105–3108 (1984).
4. X.-Y. Su, G. Von Bally, and D. Vukicevic, "Phase-stepping grating profilometry: utilization of intensity modulation analysis in complex objects evaluation," Opt. Commun. **98**, 141–150 (1993).
5. S. Zhang and S.-T. Yau, "High-resolution, real-time 3D absolute coordinate measurement based on a phase-shifting method," Opt. Express **14**, 2644–2649 (2006).
6. P. S. Huang and S. Zhang, "Fast three-step phase-shifting algorithm," Appl. Opt. **45**, 5086–5091 (2006).
7. M. Takeda and K. Mutoh, "Fourier transform profilometry for the automatic measurement of 3-D object shapes," Appl. Opt. **22**, 3977–3982 (1983).
8. X. Su and Q. Zhang, "Dynamic 3-D shape measurement method: a review," Opt. Laser Eng. **48**, 191–204 (2010).
9. M. Takeda, H. Ina, and S. Kobayashi, "Fourier-transform method of fringe-pattern analysis for computer-based topography and interferometry," J. Opt. Soc. Am. **72**, 156–160 (1982).
10. Z. Zhang, Z. Jing, Z. Wang, and D. Kuang, "Comparison of Fourier transform, windowed Fourier transform, and wavelet transform methods for phase calculation at discontinuities in fringe projection profilometry," Opt. Lasers Eng. **50**, 1152–1160 (2012).
11. R. M. Goldstein, H. A. Zebker, and C. L. Werner, "Satellite radar interferometry: two-dimensional phase unwrapping," Radio Sci. **23**, 713–720 (1988).
12. D. C. Ghiglia and M. D. Pritt, *Two-dimensional Phase Unwrapping: Theory, Algorithms, and Software* (Wiley, 1998), Vol. **4**.
13. J. M. Huntley and H. Saldner, "Temporal phase-unwrapping algorithm for automated interferogram analysis," Appl. Opt. **32**, 3047–3052 (1993).
14. S. Zhang, D. Van Der Weide, and J. Oliver, "Superfast phase-shifting method for 3-D shape measurement," Opt. Express **18**, 9684–9689 (2010).
15. K. Chen, J. Xi, Y. Yu, and L. Song, "A composite quality-guided phase unwrapping algorithm for fast 3D profile measurement," Proc. SPIE **8563**, 856305 (2012).

16. M. A. Herráez, D. R. Burton, M. J. Lalor, and M. A. Gdeisat, "Fast two-dimensional phase-unwrapping algorithm based on sorting by reliability following a noncontinuous path," Appl. Opt. **41**, 7437–7444 (2002).
17. C. Zuo, L. Huang, M. Zhang, Q. Chen, and A. Asundi, "Temporal phase unwrapping algorithms for fringe projection profilometry: a comparative review," Opt. Lasers Eng. **85**, 84–103 (2016).
18. K. Creath, "Step height measurement using two-wavelength phase-shifting interferometry," Appl. Opt. **26**, 2810–2816 (1987).
19. H. O. Saldner and J. M. Huntley, "Temporal phase unwrapping: application to surface profiling of discontinuous objects," Appl. Opt. **36**, 2770–2775 (1997).
20. G. Sansoni, M. Carocci, and R. Rodella, "Three-dimensional vision based on a combination of gray-code and phase-shift light projection: analysis and compensation of the systematic errors," Appl. Opt. **38**, 6565–6573 (1999).
21. C. Zuo, Q. Chen, G. Gu, S. Feng, F. Feng, R. Li, and G. Shen, "High-speed three-dimensional shape measurement for dynamic scenes using bi-frequency tripolar pulse-width-modulation fringe projection," Opt. Lasers Eng. **51**, 953–960 (2013).
22. K. Liu, Y. Wang, D. L. Lau, Q. Hao, and L. G. Hassebrook, "Dual-frequency pattern scheme for high-speed 3-D shape measurement," Opt. Express **18**, 5229–5244 (2010).
23. C. Zuo, Q. Chen, G. Gu, S. Feng, and F. Feng, "High-speed three-dimensional profilometry for multiple objects with complex shapes," Opt. Express **20**, 19493–19510 (2012).
24. Y. Zhang, Z. Xiong, and F. Wu, "Unambiguous 3D measurement from speckle-embedded fringe," Appl. Opt. **52**, 7797–7805 (2013).
25. T. Tao, Q. Chen, J. Da, S. Feng, Y. Hu, and C. Zuo, "Real-time 3-D shape measurement with composite phase-shifting fringes and multi-view system," Opt. Express **24**, 20253–20269 (2016).
26. X. Su and W. Chen, "Fourier transform profilometry: a review," Opt. Lasers Eng. **35**, 263–284 (2001).
27. L. Guo, X. Su, and J. Li, "Improved Fourier transform profilometry for the automatic measurement of 3d object shapes," Opt. Eng. **29**, 1439–1444 (1990).
28. C. Zuo, T. Tao, S. Feng, L. Huang, A. Asundi, and Q. Chen, "Micro Fourier transform profilometry (μftp): 3D shape measurement at 10,000 frames per second," Opt. Lasers Eng. **102**, 70–91 (2018).
29. T. Petković, T. Pribanić, and M. Đonlić, "Temporal phase unwrapping using orthographic projection," Opt. Lasers Eng. **90**, 34–47 (2017).
30. Y. Hu, Q. Chen, T. Tao, H. Li, and C. Zuo, "Absolute three-dimensional micro surface profile measurement based on a Greenough-type stereomicroscope," Meas. Sci. Technol. **28**, 045004 (2017).